PAPER

Effect of gas flow on a helium/oxygen endoscopic plasma jet

IOP Publishing Journal of Physics D: Applied Physics
J. Phys. D: Appl. Phys. **55** (2022) 415202 (12pp) https://doi.org/10.1088/1361-6463/ac7f03

Effect of gas flow on a helium/oxygen endoscopic plasma jet

Max Thulliez[1,2,*], Orianne Bastin[1,2], Antoine Remy[2], Antoine Nonclercq[1], Jacques Devière[3], Alain Delchambre[1] and François Reniers[2,*]

[1] Bio-, Electro- and Mechanical- Systems (BEAMS), Biomed Group, Ecole Polytechnique de Bruxelles, Brussels, Belgium
[2] Chemistry of Surfaces, Interfaces, and Nanomaterials, ChemSIN, Université Libre de Bruxelles, Faculty of Sciences, Brussels, Belgium
[3] Department of Gastroenterology, Hepatopancreatology, and Digestive Oncology, C.U.B. Erasme Hospital, Université Libre de Bruxelles, Brussels, Belgium

E-mail: Max.Thulliez@ulb.be and Francois.Reniers@ulb.be

Received 17 May 2022, revised 23 June 2022
Accepted for publication 6 July 2022
Published 11 August 2022

Abstract

This experimental study characterized the effect of carrier gas flow on an endoscopic plasma jet. This system generates and transports helium plasma in a tube over several meters, along with a separate channel transporting oxygen to enhance plasma reactivity on site. The resulting plasma plume exiting the tube allows treatment of tissue surfaces in an endoscopic setting with a view to perform therapeutic operations in the gastrointestinal tract. In a closed cavity simulating the tract, the carrier gas flow was studied by a combined approach investigating plasma plume chemistry, fluid dynamics, and plasma effects on the surface of a hydrogel tissue model reporting oxidation. These three aspects are shown to be closely inter-related. Plasma plume length, intensity, and shape strongly depend on helium content, velocity, turbulence, and environment. Optical emission spectroscopy was used to show that the helium gas flow rate increases the amount of helium and reactive oxygen species (ROS) in the plume. Schlieren imaging was used to visualize the transition of the fluid from buoyant to laminar and finally turbulent depending on flow rate, with a backflow in a closed cavity. Finally, the frontal and radial treatment of the cavity was assessed by measuring ROS delivery to a KI-starch agarose gel model. Helium flow rate had a noticeable effect on the treatment distribution profile and treatment intensity, with different maxima for frontal and radial treatments. This combined approach, in an accurate simulation of the target configuration (i.e. a closed, cylindrical cavity), is necessary to optimize treatment, as its outcome depends on a balance between ROS production, transport, and distribution.

Keywords: plasma jet, endoscopy, plasma medicine, ROS, Schlieren imaging, OES, hydrogel

(Some figures may appear in colour only in the online journal)

1. Introduction

Cold atmospheric plasma (CAP) for therapeutic purposes has generated significant interest over the last two decades. Plasma medicine encompasses a wide range of applications from sterilization to tumor treatment and wound healing [1–3]. CAP mainly acts through delivery of reactive oxygen and nitrogen species (RONS) to the biological target, producing oxidative stress and inducing cell signaling [4, 5]. Depending on the dose delivered, it stimulates the target (cell proliferation, migration, adhesion, regeneration) or induces oxidative damage that can result in cell death [2, 6]. Three commercially available devices already exist [1] that target wound healing.

* Authors to whom any correspondence should be addressed.

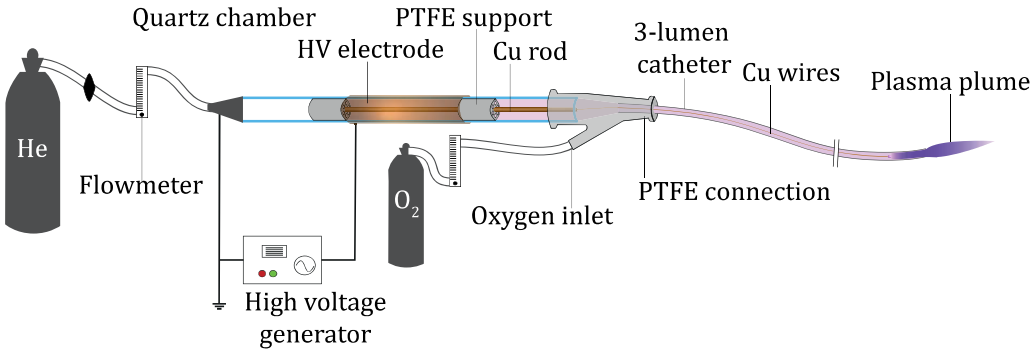

Figure 1. Plasma generation system, patented [16].

Among new applications under consideration, the use of CAP in therapeutic endoscopy appears very promising, but is also the most challenging. Indeed, while most plasma systems use CAP close to its source, a minimally invasive endoscopic CAP treatment requires transporting it internally to deliver it to the targeted tissues. This type of plasma generation and transport system has thus only been developed by a few groups [7–12]. With a view to develop potential future endoscopic applications, characterization and optimization of such systems are necessary to allow their development and ensure their safety. In this work, a helium/oxygen endoscopic plasma jet is presented, and the effect of carrier gas flow on plasma chemistry, fluid dynamics and resulting plasma treatment is characterized. Flow is particularly critical in endoscopy as CAP treatment occurs in a closed cavity. In this regard, the gas environment and fluid dynamics strongly impact the treatment. To perform the plasma characterization, plasma plume imaging was used to analyze the plume shape and intensity, and optical emission spectroscopy (OES) was used to measure plasma composition through the emissive species present in the plume. Fluid dynamics was investigated by Schlieren imaging and plasma treatment was assessed using a hydrogel tissue model combined with a reactive oxygen species (ROS) reporter based on previous work [13]. This work aimed to assess the impact of flow on CAP treatment in a setting similar to the gastrointestinal tract. It encompasses various potential therapeutic applications using CAP to produce a tissue response in the gastrointestinal wall (including the mucosa), from oxidative stimulation for regeneration or angiogenesis, to oxidative damage resulting in tissue ablation of diseased tissues (tumors, pathological mucosa). To this end, the plasma plume was placed in the center of a cylindrical closed cavity (when possible) to reproduce the gastrointestinal lumen. Both frontal (i.e. facing the plasma) and radial (i.e. parallel to the plasma) treatments were investigated. This endoscopic system is still at an early research stage and its use in human remains purely prospective as potential adverse effects of this treatment remain to be investigated.

2. Multilumen endoscopic plasma jet

The plasma generation and transport system used in this study is similar to that used in previous work [14, 15] and is represented in figure 1. A primary CAP discharge is generated through a dielectric barrier discharge (DBD) plasma jet configuration in a helium flow inside a quartz chamber. The chamber is wrapped with a copper electrode connected to an Nanosecond Pulser 120–20k high-voltage pulsed generator (settings used: 20 kV, 200 ns pulses, 2500 Hz), from Eagle Harbor Technologies. The outflow is then flushed in a polytetrafluoroethylene (PTFE) tube containing two copper wires to obtain a long plasma jet (>2 m) with a plasma plume at its exit (i.e. the visible part of the exiting plasma). These conductive wires (one in each plasma channel, as detailed hereafter) are fixed and left at floating electrical potential in the center of the discharge chamber. They extend all along the tube and transfer the primary DBD discharge to the treatment site, by acting as a counter electrode and allowing for maintenance of the plasma in an active state [14]. The wire stops a few millimeters before the tube outlet. The plasma becomes more intense, coming out to form a plume of a few centimeters.

A multilumen tube is used, i.e. a tube including three separated channels, or 'lumens'. Indeed, in most plasma medicine applications, CAP is produced in air (N_2/O_2 content), denoted hereafter as ambient air configuration. In the closed endoscopic environment (denoted as a confined atmosphere), the gas content is different but can be controlled by injecting the desired gas mix. To boost the production of RONS, crucial for the biological effect of CAP, plasma jets often use additional gases (N_2/O_2/H_2O) to tune the plasma chemistry [1]. To this end, these three lumens to allow the separated transport of helium plasma and O_2 to increase ROS production at the treatment site, as illustrated in figure 2.

Additional gases are usually directly mixed with the carrier gas [1]. They tend to destabilize the discharge due to their higher breakdown voltage and because they consume the carrier gas metastable and excited species. Electronegative gases, such as oxygen, also reduce the electron density in the plasma by attracting electrons. In the literature, oxygen additions as small as 0.5% have been reported to alter plume length in plasma jets [17]. This is especially inconvenient in the present application where the primary plasma discharge needs to be transported over several meters. Therefore, this configuration is different from conventional CAP using gas mixes. Indeed, CAP is generated here in a pure helium gas, in which high-energy metastable species are present, and mixing with O_2 occurs only later in the plasma plume as illustrated

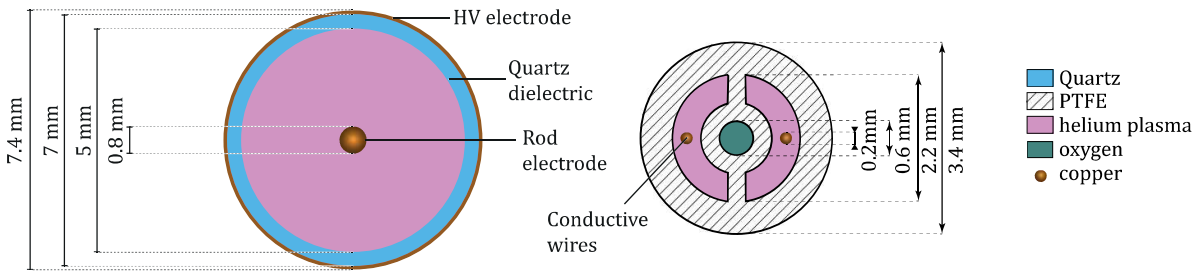

Figure 2. Discharge chamber and multilumen configuration.

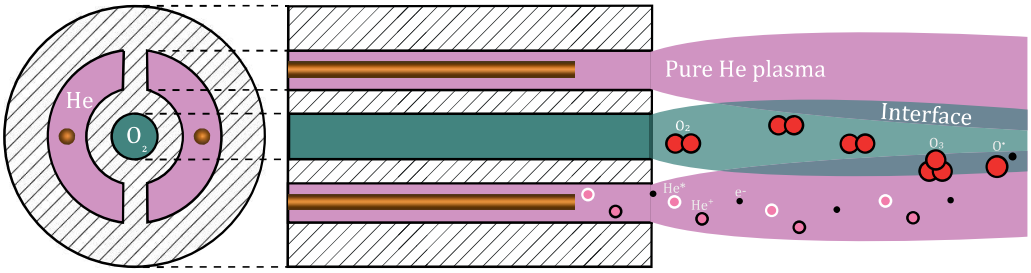

Figure 3. 2D scheme of the plasma plume mixing at the tube outlet. The separated lumens allow maintenance of a pure helium plasma that reacts with added oxygen at the interface of the two fluids.

Table 1. Summary of helium, oxygen and total flow for each condition. Flows are referred to as low, medium and high.

Flow	$1\,min^{-1}$						
	Low		Medium			High	
Helium	0	0.5	1	1.5	2	3	5
Oxygen (4%)	0	0.02	0.04	0.06	0.08	0.12	0.20
Total	0	0.52	1.04	1.56	2.08	3.12	5.20

in figure 3. In addition, this mixing is not homogeneous but rather occurs at the interface of the helium plasma and the oxygen flow, where CAP and its reactive species (RS) react with O_2 to produce ROS. Oxygen has been used in several studies to shield the plasma. It forms a peripheral 'curtain' around the plume to drastically restrict its action to a very localized zone [18–21]. In such configurations, the shielding flow consumes the plasma RONS and prevents them from spreading radially. In this work, to maximize the treatment of the surrounding walls, a reversed configuration was selected. Indeed, a central configuration of the oxygen lumen both prevents this curtain effect and deflects the helium plasma and its outflow radially.

The oxygen fraction used here thus cannot be compared to those used in the literature as they indicate the percentage of oxygen inside the CAP itself, where here it expresses a ratio between two flow rates (He and O_2) partially mixed. Here, the separation ensures the presence of a pure helium plasma inside the plume and thus of helium metastable species. In this regard, the latter can be correlated with the number of excited species, providing information about plasma chemistry and plume reactivity. The use of a symmetrical configuration ensures a homogeneous radial treatment. This mechanism highlights the importance of tuning both flow and oxygen fraction as there is a balance between decreasing plume intensity and increasing the oxygen content to maximize ROS production. This depends on plasma chemistry but also on fluid dynamics for the mixing of the helium plasma and the added oxygen.

3. Materials and methods

The impact of flow on plasma treatment was characterized using seven helium flow rates from 0 to $5\,l\,min^{-1}$ in ambient air (normal air composition) and a confined atmosphere (helium and oxygen composition depending on their respective flow rates, after a 60 s delay to establish a stable gas mix). If not stated otherwise, a 4% oxygen fraction (with respect to the helium flow rate) was maintained by concomitantly modifying the oxygen flow rate as presented in table 1.

3.1. Plasma plume imaging

Plume imaging was used to visualize the plasma plume evolution depending on the gas flow rate. Pictures were taken both in ambient air and in a confined atmosphere using a transparent glass cylinder (35 mm diameter, 65 mm length), shown in figure 4, to compare the effect of controlling the gas composition around the plume. The plasma plume was placed on a vertical test bench with a ruler for comparison. Plume

Figure 4. Setup for plume imaging in confined atmosphere. The same setup is used for imaging in ambient air with the glass container removed.

pictures were taken with a Nikon D90+ placed on a tripod in a completely dark room, in manual mode with the same settings (manual focus, ISO1000, shutter speed 1 s, aperture f8, no bracketing).

3.2. Optical emission spectroscopy

OES was used to assess the evolution of emissive RS depending on gas flow rate for wavelengths from 250 to 900 nm using a 1 s exposition. The device used in this work is an Andor Shamrock-500i spectrometer including an Andor DU420A-OE CCD camera. The analysis was performed in a closed PTFE casing (40 mm diameter, 65 mm length), with the OES probe facing the plasma plume exactly in the axis of the jet at the other extremity of the cavity (i.e. 35 mm from the plume). Five main lines of the most relevant species were selected and used for analysis, similarly to Cheng *et al* [22]: helium peak at 706 nm ($He(3^3S) \rightarrow He(2^3P)$) to assess the presence of helium excited species as it is linked to energetic electrons in atmospheric plasmas [23–25], $OH^{\bullet}$ (A–X) band at 309 nm and O peak at 777 nm ($O(^5P) \rightarrow O(^5S)$) for ROS, N_2 (C–B) second positive system band at 337 nm and N_2^+ (B–X) first negative system band at 391 nm for nitrogen reactivity.

3.3. Schlieren imaging

Schlieren imaging was used to investigate fluid dynamics which are critical in CAP chemistry (discharge type, interaction, and mixing) and RONS propagation, especially in a confined cavity and for plasma jets that specifically rely on fluid dynamics [26, 27]. The setup comprised a spherical concave mirror (160 mm diameter, 1300 mm focal distance), an LED point light source (4 V, 120 mW, cool white 9000 K) and a scalpel blade. Images were acquired using a Nikon D90+ with an 18–200 mm telephoto lens with fixed settings (manual focus on the target, ISO400, shutter speed 1/800, f5.6, no bracketing, spot metering exposure) based on Bunjong *et al* [28].

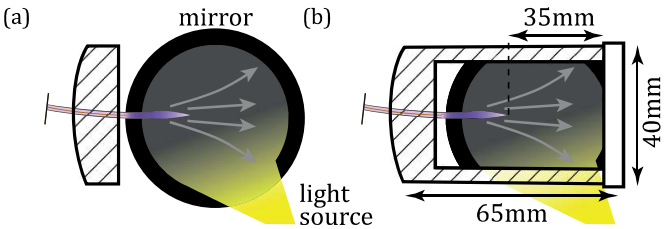

Figure 5. Schlieren imaging setup with the (a) ambient air and (b) semi-confined atmosphere setup.

The catheter was placed horizontally 50 mm in front of the mirror to observe buoyancy effects more clearly [26] with the scalpel blade parallel for optimal visualization [26]. In addition to ambient air visualization, a semi-confined setup was used with upper and lower walls and a facing petri dish (see figure 5). The diameter was selected to be close to those of the GI tract parts (esophagus, intestine) based on discussions with gastroenterologists. The length was selected to observe the evolution of the plasma plume, the fluid dynamics, and its effect on a relatively long segment. This configuration is similar to hydrogel treatment but has no vertical walls. Indeed, the use of transparent glass walls was tested but inconclusive as the refraction of glass (denser than air whereas helium flow is lighter) hides the flow. The confined atmosphere is thus not obtained but the influence of surrounding surfaces on flow can be observed.

3.4. KI-starch agarose hydrogel tissue model

A tissue model was used to efficiently map plasma action in a 3D configuration similar to the GI tract, with a target designed to mimic living tissues. Based on previous review work [13], an agarose KI-starch hydrogel reporter was used. An agarose gel of 2% weight/volume (w/v) mass fraction was selected as it has been reported to simulate soft tissues similar to mucosa, such as muscles and breasts [29–31]. A KI-starch reporter was selected with 0.3% w/v potassium iodide (KI), 0.5% w/v starch proportions based on the plasma medicine literature [20, 32–35]. This broad-spectrum colorimetric ROS reporter allows assessment of the whole oxidative power of CAP at once with high specificity (i.e. interference from other non ROS species are limited). It has been extensively used in hydrogels for plasma medicine [20, 32–46]. It is based on the iodine-starch reaction and allows the detection of most ROS (e.g. OH, O, O_3, H_2O_2, and HO_2) by changing to a blue-black color with $\lambda_{absorbance}$ around 600 nm [13, 32, 36]. As it is a critical parameter [14, 47], gel impedance was measured for several frequencies in the range relevant for this work (10–300 kHz) using an impedancemeter (WAYNEKERR Precision Component Analyzer 6425, one measurement per frequency, parallel resistor-capacitor setting) to assess whether impedance tuning was necessary. The measured conductivity in this frequency range is comprised between 1.50×10^{-1}–1.59×10^{-1} Sm^{-1}. This matches that of muscles and other soft tissues (around 10^{-1} Sm^{-1} [48, 49]) which correspond

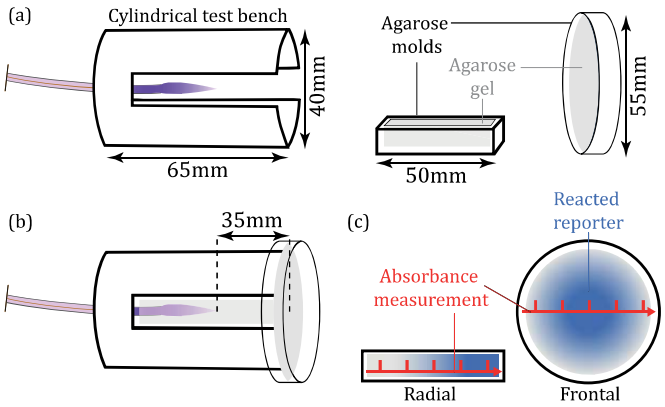

Figure 6. KI-starch agarose hydrogel tissue model with (a) the cylindrical test bench and its calibrated molds containing agarose gel, (b) closed treatment setup with the samples in place and (c) treated samples with a typical pattern of reacted reporter (blue), analyzed by absorbance in different positions (red).

to the tissues targeted in this work (i.e. gastrointestinal tract wall composed of mucosa, submucosa and muscular layers). Therefore, no tuning was required.

The gel was prepared with the compounds above in Milli-Q water, heated, and stirred on a heating plate until complete dissolution of the mixture could be observed. The solution was then poured into designated molds (at ambient temperature) to solidify. These were inserted into a cylindrical test bench mimicking an endoscopic lumen, as depicted in figure 6. The plasma plume was inserted into the center. Designated slots allow placement of two types of agarose molded samples to reproduce the GI-tract configuration: a 10 ml hydrogel sample (4.2 mm thickness) in the petri dish (55 mm diameter) facing the plasma plume at the extremity of the test bench (assessing frontal treatment) and a 5 ml hydrogel sample (10 mm thickness) in a $50 \times 10 \times 10$ mm rectangular mold slid into a slot along the length of the cylinder (assessing radial treatment). Three samples (frontal and radial) are treated for each condition. Samples are molded and treated in a randomized order. Treatment was performed for 180 s.

Measurement of treated agarose gels was achieved with absorbance spectroscopy across the sample width in different positions along the sample length (see figure 6) using a VWR UV-3100PC spectrophotometer. It was observed that ROS do not diffuse deep in the gel as only the first millimeter of gel is colored (see figure 7). Post-treatment diffusion appeared limited as no difference was observed between absorbance measurements at 0, 15, 30, 60 and 120 min. Therefore, absorbance was measured for all samples at once after treatment (<1 h). The measured absorbance can then be directly linked to the average concentration of the reacted, colored dye along the gel depth through the Beer–Lambert law [50]. The sample was placed between the light source and the spectrometer sensor using a 3D-printed bench presenting regular slots allowing movement of the sample holder by a fixed distance (5 mm). Measurements at 600 nm were repeated using the slots to obtain a profile of absorbance along the length of the sample as illustrated in figure 6.

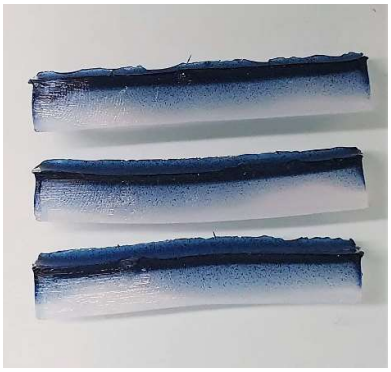

Figure 7. Side view of radial sample triplicates.

4. Results and discussion

4.1. Plume analysis

The evolution of the plumes depending on flow rate both in ambient air and in a confined atmosphere is displayed in figure 8. To better visualize the effect of flow rate on the plasma plume shape, oxygen was not used here (in contrast to OES and agarose models).

The longest and most intense plasma plume corresponds to 1.5–2 l min^{-1}. Lower flow rates resulted in shorter plumes. For higher flow rates (3 and 5 l min^{-1}), turbulence can clearly be observed in the plume, likely explaining the progressive shortening of the plume. Indeed, turbulent flow has already been reported in the literature [51] to drastically affect plume length. The longest and most intense plasma plumes appear at slightly lower flow rates in a confined atmosphere, i.e. 1 and 1.5 l min^{-1}. For higher flow rates, concurrently with the presence of a higher helium content, the plume progressively shortens and spreads horizontally, ultimately resulting in a diffuse plasma ball rather than a plume.

Figure 9 shows OES measurements in a confined atmosphere. ROS species ($OH^\bullet$ and $O^\bullet$) and helium emissive species increase with helium gas flow rate. This rise is explained by the increasing quantity of gas that result in a higher amount of excited species, and is linked to subsequently higher light emission and metastable species content. These results are consistent with plume imaging as the total light intensity also increases with the flow rate, as the plume shortens and widens. This logically leads to higher helium and atomic oxygen $O^\bullet$ production as these gases are injected into the cavity (He/O_2). $OH^\bullet$ is also detected. It is excited by electrons [52] and probably results from the presence of humidity in the plume, coming from the gas and/or residual air in the the cavity. In contrast to helium and ROS, N_2 emissions decrease with the flow rate. As no nitrogen is injected inside the cavity, it is only present in residual air. N_2 is produced by the contact of this air with electrons (thus inside the plasma) [52]. As the increasing overpressure of the gas flow drives out more of the residual air from the cavity, its production decreases. Surprisingly, N_2^+ remains relatively constant despite the lower nitrogen content at high flow rates. As it is preferentially produced by metastable species [52], it is hypothesized that the decrease of residual air

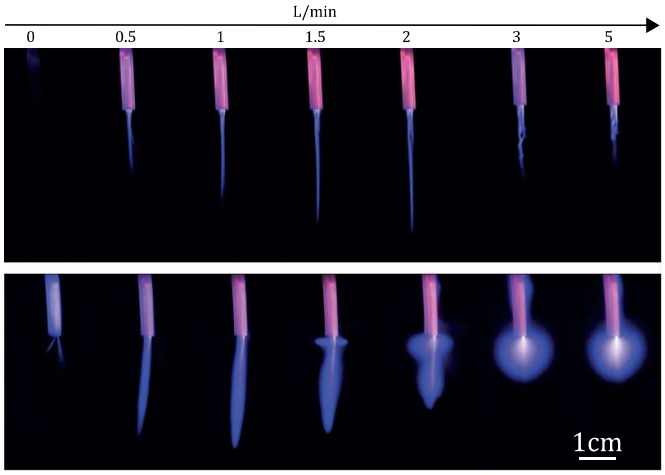

Figure 8. Evolution of plasma plume in ambient (top) and confined (bottom) atmospheres for the tested flow rates (no oxygen).

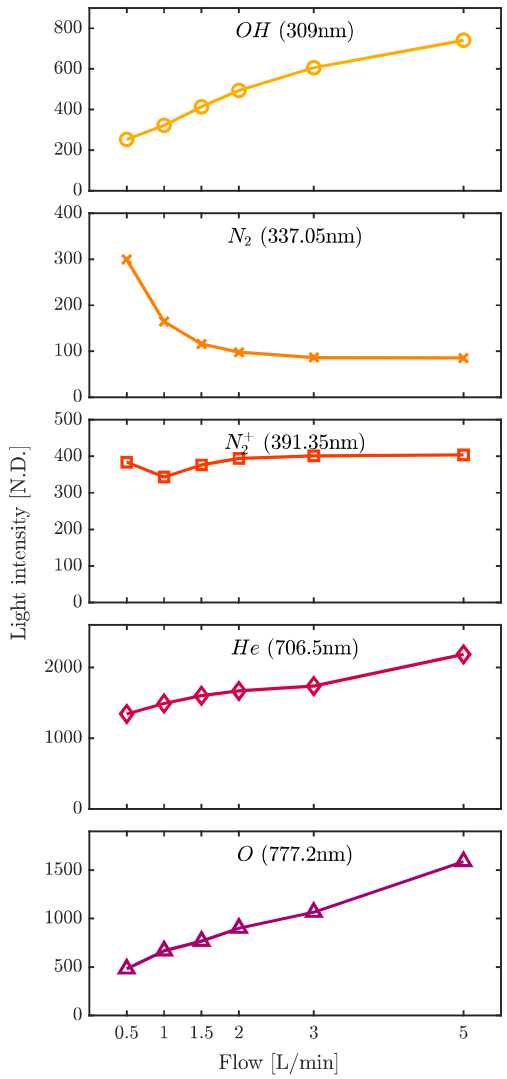

Figure 9. Evolution of emission lines of relevant RS depending on helium gas flow rate (4% oxygen fraction) in a confined atmosphere. Light intensity has no dimension (N.D.).

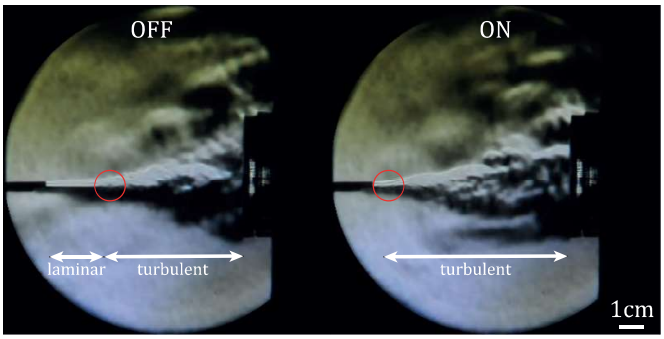

Figure 10. Plasma ignition changes fluid dynamics and reduces the laminar part of the plume before the transition point (circled in red) from 2.3 cm to a few mm. The images show a 3 l min^{-1} helium flow without (left) and with (right) plasma impinging on a floating potential target (petri dish).

in the cavity is counterbalanced by the higher metastable species content. It also suggests that the $OH^{\bullet}$ increase originates from water in the carrier gas (e.g. from the tube walls) and not in residual ambient air in the cavity. Indeed, it increases with flow rate whereas the air content (and the linked N_2 emission) decreases. This suggests that the flow rate increases the amount of electrons in the plume, producing more $OH^{\bullet}$.

In conclusion, the increase in helium flow rate leads to a higher metastable species production. Subsequently, this leads to higher production of RONS. The nature of these RONS depends on the gas composition which is also influenced by the helium flow rate. Indeed, by increasing the flow rate, the proportion of RONS originating from the injected flow (He/O_2) also increases. However, the presence of residual air and water in the gas results in $OH^{\bullet}$ and N_2^+ production even at high flow rates, as reported by Thiyagarajan *et al* [17].

4.2. Flow analysis

Inside the lumen, the helium flow is laminar for all flows (maximum Reynolds number value is 317 for 5 l min^{-1}). After it exits, the flow is strongly influenced by the surrounding fluids, including those present around the jet and the added oxygen gas flow.

The plasma ignition affected the flow regime by reducing the distance between the exit nozzle and the place where the laminar flow exiting from the tube makes a transition to turbulent (figure 10). The displacement of this so-called 'transition point' has already been reported for classical plasma jets [27, 53, 54]. It is caused by the interaction of the charged species with the gas flow. Several potential explanations include localized heating of the gas that is producing a faster stream [27], and movement of ions due to electrodynamic forces in the jet (traveling electric fields, propagation of an ionization wave) that impart momentum to neutral species in the flow through collisions [27, 53, 54]. This effect is particularly important for low flow rates as higher flow rates show a transition point naturally closer to the tube exit (figure 11).

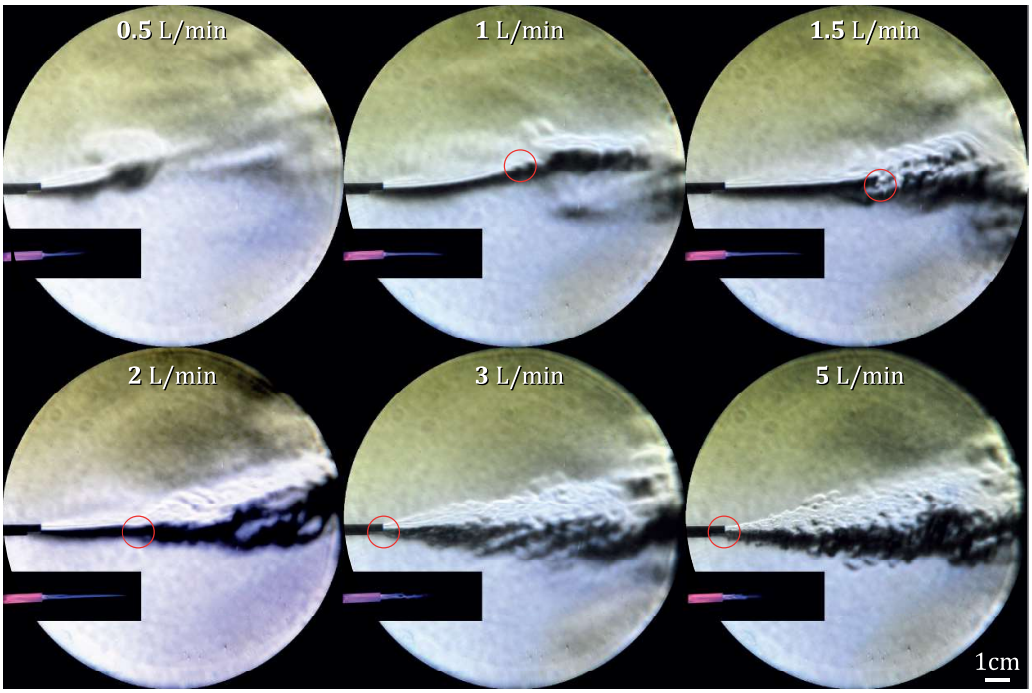

Figure 11. Impact of flow rate on fluid dynamics in a pure helium plasma plume (no oxygen) in ambient air. Plasma plumes from figure 8 are superimposed as a reference at the same scale. Transition points are circled in red (if the transition occurs).

The flow regime is particularly important for ROS production and distribution. Indeed, in the laminar zone, there is little mixing between the helium plasma RS and the surrounding gases, i.e. ambient gas and injected gas: air and O_2, respectively, in ambient air, He/O_2 and O_2, respectively, in a confined atmosphere. The opening angle of the helium outflow is very low and the radial velocity of the flow is almost non-existent, resulting in a very directional flow. After the transition point, the flow becomes turbulent, and the mixing and distribution of the flow are then significantly increased.

The evolution of fluid dynamics depending on flow in ambient air is displayed in figure 11, along with the corresponding images of the plasma plumes. At low flow rates, the buoyancy effect of the lighter helium has a strong influence on flow morphology with the flow path drifting upwards similarly to that observed by Jiang *et al* [55]. In general, this buoyancy is important in helium plasma jets [54, 55] as it brings the RONS upwards. This vertical drag has been shown to strongly impact treatment by Liu *et al* [45], notably by the angle between the target and the plasma plume. When increasing the flow rate, a turbulent zone appears at $1.5\,l\,min^{-1}$, then the transition point moves closer to the outlet until the flow becomes exclusively turbulent at $3\,l\,min^{-1}$, in agreement with the plasma plume images (figure 8). For low flow rates (0.5 and $1\,l\,min^{-1}$) a laminar but short plasma plume is observed due to the lower quantity of helium excited species and the lower velocity of the gas bringing them forward. For mid-range values (1.5 and $2\,l\,min^{-1}$) the balance between helium quantity and velocity produces the longest plumes as the turbulent zone appears after the plume. Then, the turbulence reduces the forward velocity for high flow rates (3 and $5\,l\,min^{-1}$). It also quickly consumes the helium excited species as they react because of higher mixing between the different flows (helium plasma, additional oxygen, ambient air). This results in shorter, more turbulent plumes.

It is also interesting to observe that the flow propagates considerably farther than the plume. This is critical for treating large surfaces as the flow brings the RONS along and allows them to be distributed outside the very limited plume region. Indeed, Oh *et al* have shown that the surfaces outside the plume but in contact with the outflow transporting the RONS are affected, meaning that CAP treatment does reach an area larger than the visible plasma plume [56].

The evolution of fluid dynamics depending on flow in a semi-confined atmosphere is displayed in figure 12. This semi-confined setup does not fully recapitulate the gas conditions of a confined atmosphere (i.e. He/O_2 saturated atmosphere resulting in a diffuse plasma). However, it was used to evaluate the interaction of the plasma outflow with physical boundaries, i.e. the backflow of the gas impinging on the frontal target and how it propagates along walls. The tendency is similar to that observed in ambient air. A buoyancy effect is present at low flow rate but the presence of a target at a close distance (35 mm) leaves less room for upward drifting. Mid-range flow rates show almost exclusively a laminar flow before reaching the target as it is placed before the transition point. High flow rates present turbulence directly from the outlet. In contrast to ambient air, however, the presence of the target and horizontal walls forces mixing even at low flow rate when impinging on it, with a backflow of the gas.

The shape of the plasma plumes is in agreement with the flow pattern observed here. At low flow rate, the laminar flow

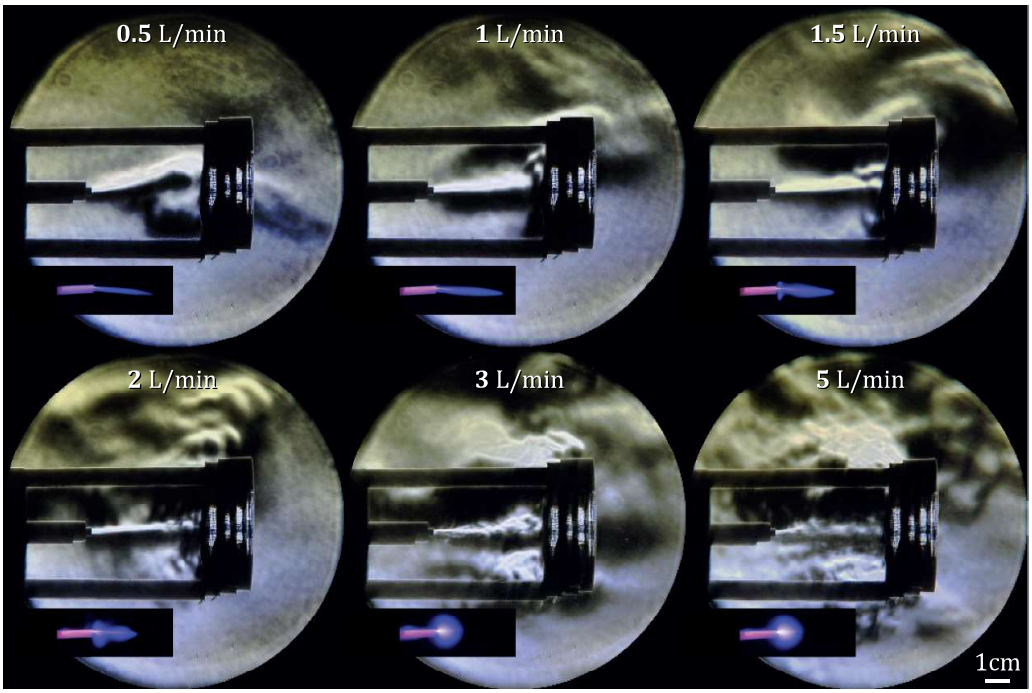

Figure 12. Impact of flow rate on fluid dynamics in a pure helium plasma plume (no oxygen) in a semi-confined cavity. Plasma plumes from figure 8 are superimposed as a reference at the same scale but are not representative of the same conditions (confined vs semi-confined, no oxygen).

results in a plasma plume that propagates almost as in ambient air. Due to the high helium content in the surroundings, its shape is wider and more diffuse because of the additional creation of helium excited species along the plume. As the flow rate increases, the forward flow path gets increasingly impaired by turbulence, backflow, and increased pressures. Consequently, the plasma reacts with the surrounding helium-rich environment. The straight, elongated part of the plume is shortened and helium excited species are created radially as the plume widens, especially at its base, to finally produce plasma balls. Indeed, the plasma ignites the helium species that are closest to the tube outlet and no longer straight ahead.

The presence of a sufficiently reactive plume, combined with a high production and distribution of RONS (potentially through turbulence and backflow to allow mixing) is critical for treatment. Indeed, the turbulent outflow of the jet allows it to reach surfaces outside the plume [56]. In addition, the relatively low impedance of the tissues (or hydrogels) may enhance RONS delivery as the target impedance impacts not only the plasma plume but also the flow. Indeed Robert *et al* have demonstrated that a plasma plume impinging on a grounded target brings the helium flow towards the target. In contrast, its buoyancy makes it flow upwards before the target when it is not connected grounded [54].

4.3. Effect on gel model

4.3.1. Absorbance profile. The absorbance profiles are shown in figure 13. H_2O_2 calibration on the same model is superimposed as a reference. However, multiple absorbance measurements ($A > 2$) were outside of the Beer–Lambert linear zone [50]. Therefore, these results cannot be directly linked to the concentration of reacted reporter, but still provide a qualitative indication to compare the oxidative power of each condition. Both frontal and radial treatments proved to be relatively non-homogeneous along their length as confirmed by absorbance measurements.

4.3.1.1. For frontal treatment. The inhomogeneity logically consists of a maximal treatment in the center of the sample, gradually decreasing along its radius. Indeed, this zone directly faces the plasma plume and thus receives the highest amount of ROS. Other ROS also reach the rest of the sample, with a concentration gradually decreasing with the distance from the plume. The profiles show a very low treatment at $0\,1\,\mathrm{min}^{-1}$ and a decrease at high flow rates. For $0\,1\,\mathrm{min}^{-1}$, no gas is injected in the system but some plasma can, however, still be observed (as presented in figure 8) by ionization of the surrounding air by corona effect. Flow rates around $1–1.5\,1\,\mathrm{min}^{-1}$ produce the strongest frontal treatment in almost all positions but also a more homogeneous, bell-shaped treatment. In contrast, high flow rates show a sharper profile, indicating a more localized treatment, i.e. intermediary positions (± 0.5 to ± 1.5 cm) are less impacted. This indicates that, despite the higher mixing observed by Schlieren imaging and on the turbulent plasma plumes, high flow rates do not produce more ROS and bring them straight, to the center of the dish.

4.3.1.2. For radial treatment. Inhomogeneity is observed along the sample. The extremity farthest from the nozzle corresponds to the highest treatment, in agreement with what

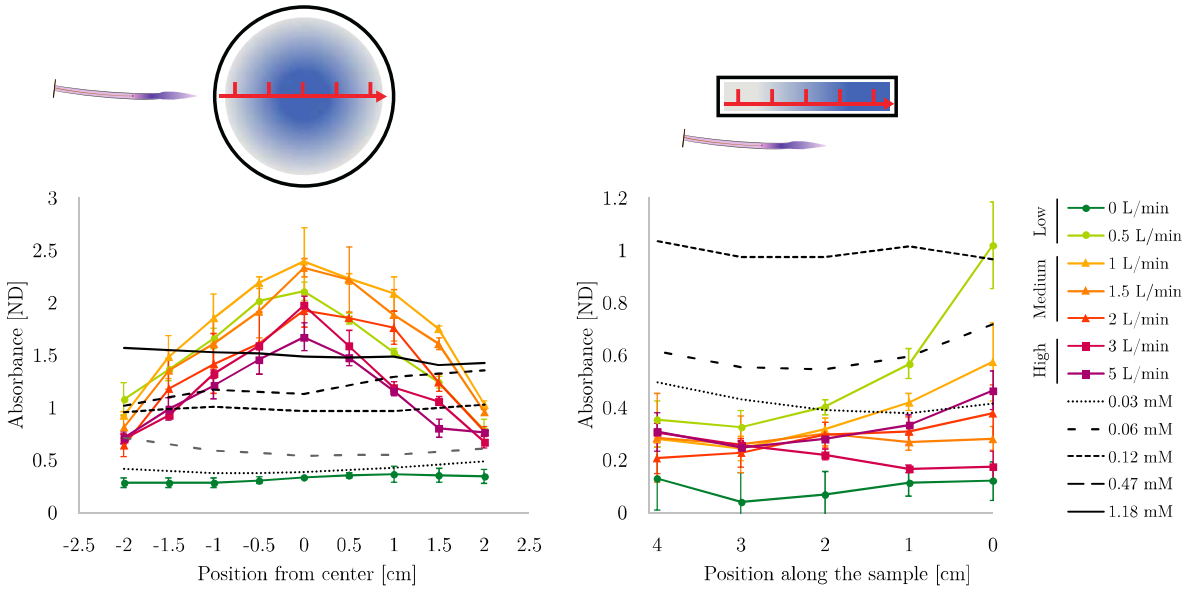

Figure 13. Absorbance profile of frontal (left) and radial (right) treatment depending on helium gas flow rate (4% oxygen fraction). Calibration samples treated with various H_2O_2 doses are given as a landmark in black. Error bars show standard deviation computed on triplicates. Absorbance has no dimension (ND).

is observed in Schlieren imaging. After impacting the petri dish, the helium flow spreads radially to backflow from this extremity to the other end along the rectangular molds, bringing ROS to the gel. The farthest positions are touched first, resulting in a stronger treatment. This is similar to what was described in the computational modeling study from PLASMANT [57]. The inhomogeneity is greater at low flow rate, as the backflow is weaker (see figure 12), probably resulting in a slower ROS circulation toward the upstream extremity of the rectangular mold and stagnation of ROS at the positions farthest from the plume.

4.3.2. Absorbance intensity. The absorbance values obtained for each sample were averaged over the entire sample to provide a mean absorbance allowing assessment of global treatment intensity (i.e. total ROS delivery). The evolution of the mean absorbance is shown in figure 14.

4.3.2.1. For frontal treatment. Flow rates around $1\,l\,min^{-1}$ result in a stronger mean treatment. This is in agreement with plume imaging as these flow rates correspond to the longest, most laminar plasma plumes in a confined atmosphere, i.e. the conditions presenting the most helium RS (including excited species and metastable species) and thus bringing the most ROS toward the frontal sample. In terms of ROS delivery, a mean absorbance of 1.5 corresponds to a 1.18 mM concentration of H_2O_2.

4.3.2.2. For radial treatment. The most effective flow rate (in terms of treatment intensity) is clearly $0.5\,l\,min^{-1}$, in contrast to frontal treatment. A possible explanation is that this low flow rate does not bring all ROS forward toward the frontal sample, but rather allows them to reach the walls directly. This

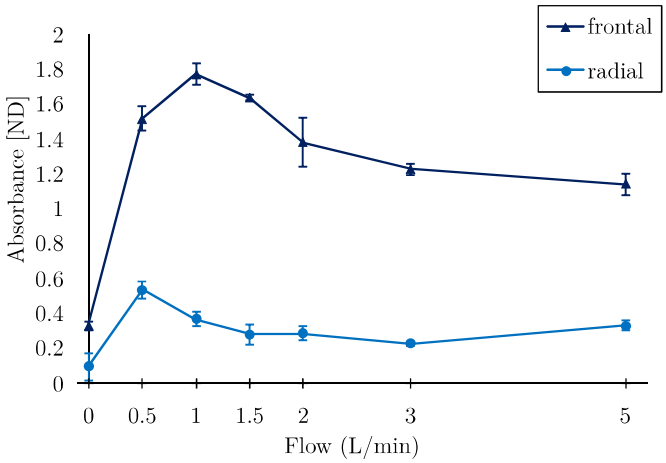

Figure 14. Mean absorbance along sample of frontal and radial treatment depending on flow rate. Error bars show standard deviation computed on triplicates. Absorbance has no dimension (ND).

shorter plume presents fewer helium RS and a low mixing but the ROS that are created are delivered directly to the radial samples rather than through the backflow, where only a few remain after contact with the frontal sample. This shows that long plumes, mixing, and turbulence might not be particularly beneficial to increase radial treatment. With an absorbance of around 0.5, this can be compared to a concentration between 0.03 mM and 0.06 mM H_2O_2, significantly lower than for frontal treatment.

4.4. Overall discussion

For both radial and frontal treatments, OES does not predict CAP treatment intensity. It does not correlate directly with

CAP treatment for two main reasons. OES identifies emissive species only and is thus not a direct indicator of optimal reactivity but rather allows for a partial characterization of RS and an indication of what species are formed. Indeed, a higher light intensity at a specific wavelength (here 706, 309, 777, 337, and 391 nm) indicates the presence of a higher amount of the corresponding emissive species in the plume (He, $OH^{\bullet}$, O, N_2, and N_2^+ respectively). However, it does not account for other RS which do not emit light, such as hydrogen peroxide H_2O_2, ozone O_3 or metastable atomic oxygen $O^{\bullet}$. These, on the other hand, are detected by the hydrogel model. OES characterizes the species inside the plume but this does not necessarily mean these species reach the walls (i.e. the tissue or the gel), either because they react beforehand or because the flow does not transport them there. Typically, the mean free path of these emissive RS present in the plume decreases with the flow rate as the velocity increase, reducing their range of action. This highlights the gap between OES measurements and CAP treatment. Despite its poor prediction of the final treatment outcome, this technique provides a better understanding of plasma plume chemistry, and how treatment parameters affect it, by providing partial information on its composition (i.e. emissive species). In this context, OES showed an increase of all relevant emissive species with carrier gas flow rate. However, the endoscopic constraints prevent the use of such high flow rates.

In addition, despite a potentially higher ROS production (no information available about non-emissive ROS), plume and Schlieren imaging showed that the plasma plume is shortened by high flow rates due to turbulence. In addition to shortening the active region of the plasma, this turbulence impairs the diffusion of ROS. The combination of these two phenomena results in treatment maxima at low flow rates, which are different for frontal and radial treatment. This confirms that the treatment depends on a balance between providing enough gas to produce an intense plasma (with enough helium RS) and finding the optimal gas flow rate to both produce enough ROS and distribute them depending on the desired target (i.e. frontal or radial). For frontal treatment, the longest plume, appearing at $1\,l\,min^{-1}$, maximizes the amount of helium RS (and resulting ROS) moving forward and treating the sample, and is therefore optimal. Above this value, the turbulence reduces plume length and impairs forward delivery of ROS quite clearly, since flow rates above $2\,l\,min^{-1}$ (which are clearly less effective) correspond to the appearance of turbulent flow (figure 12). For radial treatment, ROS can either be delivered directly by diffusion or through backflow, the latter appearing to be less effective. This favors a low flow rate of $0.5\,l\,min^{-1}$. However, it provides more heterogeneity as the distribution mechanism of RS (direct and low backflow) results in less ROS circulation. Nevertheless, this relatively non-homogeneous profile seems acceptable, as $0.5\,l\,min^{-1}$ clearly produces the strongest radial treatment in terms of overall ROS delivery. In addition, it is more convenient to use lower flow rates in the constrained endoscopic environment. However, it is realistic to expect that this optimal flow rate will vary depending on the dimensions of the cavity (i.e. its diameter). In contrast to what has been suggested by plume imaging (figure 8), wide plasma plumes do not result in better radial treatment and are merely the consequence of turbulence. The latter also appears not to be beneficial as it does not increase ROS production but rather impairs their delivery.

These experiments confirm the mismatch between OES and CAP treatment and highlight the importance of Schlieren imaging and hydrogels to understand and predict plasma reactivity. Significant research is still required to consider endoscopic applications in order to ensure an optimal and safe treatment.

5. Conclusion

This work has clarified the process of ROS production and distribution of an endoscopic plasma jet in a closed cavity and semi-closed cavity. Its multilumen configuration allows maintenance of a pure helium plasma to the treatment site, where it is mixed with oxygen to enhance and maximize ROS production. Plume imaging showed that carrier gas flow rate impacts plume length, shape, and intensity to produce the strongest plasma plume at medium flow rate, when the helium content and velocity are sufficient but not yet impaired by turbulence. In addition, a confined atmosphere allows for control of the gas environment, with a high content helium flow producing a more diffuse plume. OES showed that higher gas flow rates, combined with the added oxygen, produce more helium and ROS emissive species. However, these results do not predict treatment outcome on a hydrogel tissue model. Schlieren imaging highlighted the crucial role of fluid dynamics for plasma treatment in this configuration, with turbulence appearing as an unwanted effect. Finally, assessment of the CAP effect on surfaces allowed for identification of different optimal flow rates to maximize frontal and radial treatments in this setup (i.e. with these specific cavity dimensions). Indeed, a balance between helium metastable species, mixing and distribution in the cavity must be made to obtain good treatment intensity and distribution, in a combination depending on the targeted area. These experiments demonstrate the importance of a combined approach in the characterization of such systems, including plasma chemistry, fluid dynamics, and measurement of treatment on surfaces and also supported the need to better simulate the targeted environment, i.e. its configuration, dimensions, composition and impedance.

Data availability statement

The data that support the findings of this study are available upon reasonable request from the authors.

Acknowledgments

This work was supported by the Fondation Michel Cremer. The authors acknowledge the contribution of a medical writer, Sandy Field, PhD, for English language editing of this manuscript.

ORCID iDs

Max Thulliez https://orcid.org/0000-0001-9614-3417
Orianne Bastin https://orcid.org/0000-0003-4993-3525
Antoine Nonclercq https://orcid.org/0000-0003-0292-9588
Jacques Devière https://orcid.org/0000-0003-1889-1924
Alain Delchambre https://orcid.org/0000-0002-6047-1002
François Reniers https://orcid.org/0000-0001-9331-6060

References

[1] Metelmann H-R, Von Woedtke T and Weltmann K-D 2018 *Comprehensive Clinical Plasma Medicine* (Berlin: Springer)
[2] Metelmann H-R *et al* 2018 Clinical experience with cold plasma in the treatment of locally advanced head and neck cancer *Clin. Plasma Med.* **9** 6–13
[3] Braný D, Dvorská D, Halašová E and Škovierová H 2020 Cold atmospheric plasma: a powerful tool for modern medicine *Int. J. Mol. Sci.* **21** 2932
[4] Laroussi M 2009 Low-temperature plasmas for medicine? *IEEE Trans. Plasma Sci.* **37** 714–25
[5] Graves D B 2012 The emerging role of reactive oxygen and nitrogen species in redox biology and some implications for plasma applications to medicine and biology *J. Phys. D: Appl. Phys.* **45** 263001
[6] Von Woedtke T, Reuter S, Masur K and Weltmann K-D 2013 Plasmas for medicine *Phys. Rep.* **530** 291–320
[7] Robert E, Barbosa E, Dozias S, Vandamme M, Cachoncinlle C, Viladrosa R and Pouvesle J M 2009 Experimental study of a compact nanosecond plasma gun *Plasma Process. Polym.* **6** 795–802
[8] Kim J Y, Kim S-O, Wei Y and Li J 2010 A flexible cold microplasma jet using biocompatible dielectric tubes for cancer therapy *Appl. Phys. Lett.* **96** 203701
[9] Polak M, Winter J, Schnabel U, Ehlbeck J and Weltmann K D 2012 Innovative plasma generation in flexible biopsy channels for inner-tube decontamination and medical applications *Plasma Process. Polym.* **9** 67–76
[10] Kostov K G, Machida M and Prysiazhnyi V 2012 Generation of cold argon plasma jet at the end of flexible plastic tube (arXiv:1411.3976 [physics.plasm-ph])
[11] Robert E *et al* 2013 Perspectives of endoscopic plasma applications *Clin. Plasma Med.* **1** 8–16
[12] Kurosawa M, Takamatsu T, Kawano H, Hayashi Y, Miyahara H, Ota S, Okino A and Yoshida M 2019 Endoscopic hemostasis in porcine gastrointestinal tract using CO_2 low-temperature plasma jet *J. Surg. Res.* **234** 334–42
[13] Thulliez M, Bastin O, Nonclercq A, Delchambre A and Reniers F 2021 Gel models to assess distribution and diffusion of reactive species from cold atmospheric plasma: an overview for plasma medicine applications *J. Phys. D: Appl. Phys.* **54** 463001
[14] Bastin O, Thulliez M, Servais J, Nonclercq A, Delchambre A, Hadefi A, Devière J and Reniers F 2020 Optical and electrical characteristics of an endoscopic DBD plasma jet *Plasma Med.* **10** 71–90
[15] Bastin O, Thulliez M, Delchambre A, Devière J, Reniers F and Nonclercq A 2022 Nanopulsed long DBD plasma jet: excitation voltage parameters to increase plasma reactivity *J. Phys. D: Appl. Phys.* (in review)
[16] Bastin O *et al* 2019 *Device for cold plasma treatment and cold plasma endoscopic system* EP3914174A1
[17] Thiyagarajan M, Sarani A and Nicula C 2013 Optical emission spectroscopic diagnostics of a non-thermal atmospheric pressure helium-oxygen plasma jet for biomedical applications *J. Appl. Phys.* **113** 233302
[18] Reuter S, Winter J, Schmidt-Bleker A, Tresp H, Hammer M U and Weltmann K D 2012 Controlling the ambient air affected reactive species composition in the effluent of an argon plasma jet *IEEE Trans. Plasma Sci.* **40** 2788–94
[19] Winter J, Nishime T M C, Glitsch S, Lühder H and Weltmann K D 2018 On the development of a deployable cold plasma endoscope *Contrib. Plasma Phys.* **58** 404–14
[20] Kapaldo J, Han X and Ptasinska S 2019 Shielding-gas-controlled atmospheric pressure plasma jets: optical emission, reactive oxygen species and the effect on cancer cells *Plasma Process. Polym.* **16** 1–15
[21] Winter J, Nishime T M C, Bansemer R, Balazinski M, Wende K and Weltmann K D 2019 Enhanced atmospheric pressure plasma jet setup for endoscopic applications *J. Phys. D: Appl. Phys.* **52** 024005
[22] Cheng X, Sherman J, Murphy W, Ratovitski E, Canady J and Keidar M 2014 The effect of tuning cold plasma composition on glioblastoma cell viability *PLoS One* **9** e98652
[23] Nersisyan G and Graham W G 2004 Characterization of a dielectric barrier discharge operating in an open reactor with flowing helium *Plasma Sources Sci. Technol.* **13** 582
[24] Liu D W, Iza F and Kong M G 2009 Electron avalanches and diffused γ-mode in radio-frequency capacitively coupled atmospheric-pressure microplasmas *Appl. Phys. Lett.* **95** 031501
[25] Nie Q-Y, Cao Z, Ren C-S, Wang D Z and Kong M G 2009 A two-dimensional cold atmospheric plasma jet array for uniform treatment of large-area surfaces for plasma medicine *New J. Phys.* **11** 115015
[26] Traldi E, Boselli M, Simoncelli E, Stancampiano A, Gherardi M, Colombo V and Settles G S 2018 Schlieren imaging: a powerful tool for atmospheric plasma diagnostic *EPJ Tech. Instrum.* **5** 1–23
[27] Bradley J W, Oh J-S, Olabanji O T, Hale C, Mariani R and Kontis K 2011 Schlieren photography of the outflow from a plasma jet *IEEE Trans. Plasma Sci.* **39** 2312–3
[28] Bunjong D, Pussadee N and Wattanakasiwich P 2018 Optimized conditions of Schlieren photography *J. Phys.: Conf. Ser.* **1144** 012097
[29] Kato H, Kuroda M, Yoshimura K, Yoshida A, Hanamoto K, Kawasaki S, Shibuya K and Kanazawa S 2005 Composition of MRI phantom equivalent to human tissues *Med. Phys.* **32** 3199–208
[30] Dobrynin D, Fridman G, Friedman G and Fridman A 2012 Deep penetration into tissues of reactive oxygen species generated in floating-electrode dielectric barrier discharge (FE-DBD): an *in vitro* agarose gel model mimicking an open wound *Plasma Med.* **2** 71–83
[31] Zell K, Sperl J I, Vogel M W, Niessner R and Haisch C 2007 Acoustical properties of selected tissue phantom materials for ultrasound imaging *Phys. Med. Biol.* **52** N475–84
[32] Kawasaki T, Kawano K, Mizoguchi H, Yano Y, Yamashita K, Sakai M, Shimizu T, Uchida G, Koga K and Shiratani M 2014 Visualization of the distribution of oxidizing substances in an atmospheric pressure plasma jet *IEEE Trans. Plasma Sci.* **42** 2482–3
[33] Kawasaki T, Mitsugi F, Koga K and Shiratani M 2019 Local supply of reactive oxygen species into a tissue model by atmospheric-pressure plasma-jet exposure *J. Appl. Phys.* **125** 213303
[34] Omran A, Busco G, Dozias S, Grillon C, Valinataj Omran A, Busco G, Dozias S, Pouvesle J-M and Robert E 2019 Distribution and penetration of reactive oxygen and nitrogen species through a tissue phantom after plasma gun

treatment *24th Int. Symp. on Plasma Chemistry (ISPC24)* (*Naples, June 2019*) (available at: https://hal.archives-ouvertes.fr/hal-02263879)

[35] Ghimire B, Szili E J, Lamichhane P, Short R D, Lim J S, Attri P, Masur K, Weltmann K D, Hong S H and Choi E H 2019 The role of UV photolysis and molecular transport in the generation of reactive species in a tissue model with a cold atmospheric pressure plasma jet *Appl. Phys. Lett.* **114** 093701

[36] Nakajima A, Uchida G, Kawasaki T, Koga K, Sarinont T, Amano T, Takenaka K, Shiratani M and Setsuhara Y 2015 Effects of gas flow on oxidation reaction in liquid induced by He/O_2 plasma-jet irradiation *J. Appl. Phys.* **118** 043301

[37] Uchida G, Nakajima A, Ito T, Takenaka K, Kawasaki T, Koga K, Shiratani M and Setsuhara Y 2016 Effects of nonthermal plasma jet irradiation on the selective production of H_2O_2 and NO_2^- in liquid water *J. Appl. Phys.* **120** 203302

[38] Kawasaki T, Eto W, Hamada M, Wakabayashi Y, Abe Y and Kihara K 2015 Detection of reactive oxygen species supplied into the water bottom by atmospheric non-thermal plasma jet using iodine-starch reaction *Jpn. J. Appl. Phys.* **54** 086201

[39] Kawasaki T, Kusumegi S, Kudo A, Sakanoshita T, Tsurumaru T, Sato A, Uchida G, Koga K and Shiratani M 2016 Effects of irradiation distance on supply of reactive oxygen species to the bottom of a Petri dish filled with liquid by an atmospheric O_2/He plasma jet *J. Appl. Phys.* **119** 173301

[40] Kawasaki T, Kusumegi S, Kudo A, Sakanoshita T, Tsurumaru T and Sato A 2016 Effects of gas flow rate on supply of reactive oxygen species into a target through liquid layer in cold plasma jet *IEEE Trans. Plasma Sci.* **44** 3223–9

[41] Kawasaki T, Kawano K, Mizoguchi H, Yano Y, Yamashita K and Sakai M 2016 Visualization of the two-dimensional distribution of ROS supplied to a water-containing target by a non-thermal plasma jet *Int. J. Plasma Environ. Sci. Technol.* **10** 41–46

[42] Kawasaki T, Sato A, Kusumegi S, Kudo A, Sakanoshita T, Tsurumaru T, Uchida G, Koga K and Shiratani M 2016 Two-dimensional concentration distribution of reactive oxygen species transported through a tissue phantom by atmospheric-pressure plasma-jet irradiation *Appl. Phys. Express* **9** 076202

[43] Kawasaki T, Nishida K, Uchida G, Mitsugi F, Takenaka K, Koga K, Setsuhara Y and Shiratani M 2020 Effects of surrounding gas on plasma-induced downward liquid flow *Jpn. J. Appl. Phys.* **59** SHHF02

[44] He T, Liu D, Liu Z, Wang S, Liu Z, Rong M and Kong M G 2019 Transportation of ROS in model tissues treated by an Ar + O_2 plasma jet *J. Phys. D: Appl. Phys.* **52** 045204

[45] Liu D, He T, Liu Z, Wang S, Liu Z, Rong M and Kong M G 2018 Spatial-temporal distributions of ROS in model tissues treated by a He + O_2 plasma jet *Plasma Process. Polym.* **15** 1800057

[46] Mitsugi F, Kusumegi S and Kawasaki T 2019 Visualization of ROS distribution generated by atmospheric plasma jet *IEEE Trans. Plasma Sci.* **47** 1057–62

[47] Stancampiano A, Chung T-H, Dozias S, Pouvesle J-M, Mir L M and Robert E 2019 Mimicking of human body electrical characteristic for easier translation of plasma biomedical studies to clinical applications *IEEE Trans. Radiat. Plasma Med. Sci.* **4** 335–42

[48] Gabriel C, Gabriel S and Corthout Y E 1996 The dielectric properties of biological tissues: I. Literature survey *Phys. Med. Biol.* **41** 2231

[49] Grimnes S and Martinsen O G 2011 *Bioimpedance and Bioelectricity Basics* (New York: Academic)

[50] Skoog D A, West D M, Holler F J and Crouch S R 2014 *Fundamentals of Analytical Chemistry* 9th edn, ed M Finch (Belmont, CA: Brooks/Cole)

[51] Li Q, Li J-T, Zhu W-C, Zhu Xi-M and Pu Y-K 2009 Effects of gas flow rate on the length of atmospheric pressure nonequilibrium plasma jets *Appl. Phys. Lett.* **95** 141502

[52] Gazeli K, Svarnas P, Vafeas P, Papadopoulos P K, Gkelios A and Clement F 2013 Investigation on streamers propagating into a helium jet in air at atmospheric pressure: electrical and optical emission analysis *J. Appl. Phys.* **114** 103304

[53] Foletto M, Puech V, Fontane J, Joly L and Pitchford L C 2014 Evidence of the influence of plasma jets on a helium flow into open air *IEEE Trans. Plasma Sci.* **42** 2436–7

[54] Robert E, Sarron V, Darny T, Riès D, Dozias S, Fontane J, Joly L and Pouvesle J M 2014 Rare gas flow structuration in plasma jet experiments *Plasma Sources Sci. Technol.* **23** 012003

[55] Jiang N, Yang J, He F and Cao Z 2011 Interplay of discharge and gas flow in atmospheric pressure plasma jets *J. Appl. Phys.* **109** 093305

[56] Oh J-S, Olabanji O T, Hale C, Mariani R, Kontis K and Bradley J W 2011 Imaging gas and plasma interactions in the surface-chemical modification of polymers using micro-plasma jets *J. Phys. D: Appl. Phys.* **44** 155206

[57] Heirman P, Van Boxem W and Bogaerts A 2019 Reactivity and stability of plasma-generated oxygen and nitrogen species in buffered water solution: a computational study *Phys. Chem. Chem. Phys.* **21** 12881–94